26

C.E. SACLAY
DSM

SERVICE D'ÉLECTRONIQUE ET D'INFORMATIQUE

FERMILAB
FEB 12 1999
LIBRARY

DAPNIA-SEI-98-07

Fermilab Library
0 1160 0068300 7

MS

DAPNIA/SEI 98-07 December 1998

FAINT SOURCE DETECTION IN ISOCAM IMAGES WITH PRETI

RETURN TO FERMILAB LIBRARY

J.L. Starck, H. Aussel, D. Elbaz, D. Fadda, C. Cesarsky

DAPNIA

Submitted to Astronomy and Astrophysics

Couverture : Sylvie Cabrit et Marc Sauvage

Le DAPNIA (**D**épartement d'**A**strophysique, de physique des **P**articules, de physique **N**ucléaire et de l'**I**nstrumentation **A**ssociée) regroupe les activités du Service d'Astrophysique (SAp), du Département de Physique des Particules Elémentaires (DPhPE) et du Département de Physique Nucléaire (DPhN).

Adresse : DAPNIA, Bâtiment 141
CEA Saclay
F - 91191 Gif-sur-Yvette Cedex

A&A manuscript no.
(will be inserted by hand later)

Your thesaurus codes are:
03.13.2; 03.20.1;

Faint source detection in ISOCAM images with PRETI

J.L. Starck, H. Aussel, D. Elbaz, D. Fadda, and C. Cesarsky

DAPNIA/SEI-SAP, CEA-Saclay, F-91191 Gif-sur-Yvette Cedex, France

Received date; accepted date

Abstract. The aim of this paper is to describe a tool used for the detection of mid-infrared images of faint sources from the ISOCAM camera on-board ISO. This tool is based on a wavelet analysis which allows to discriminate sources from cosmic ray impacts at the very limit of the instrument, four orders of magnitudes below IRAS. The results obtained with this method, called PRETI, for Pattern REcognition Technique for ISOCAM data, will be detailed in separated papers, except for one case, the Hubble Deep Field, that we used as an example for testing this tool. We have built a set of simulated data in order to define the sensitivity and completeness limits of the observations as well as the rate of false detections due to cosmic ray impacts as a function of the detection threshold used, which was not possible at the time of the release of our first paper (Aussel *et al.* 1999). Forthcoming papers are in preparation which will all refer to the technique described in this paper with the common aim of understanding galaxy evolution through their rest-frame near to mid-infrared emission, i.e. surveys of different depths and sizes on empty fields and galaxy clusters, as well as on fields surrounding distant quasars.

1. Introduction

Following the detection of ultra-luminous infrared galaxies (ULIRG's) by the IRAS satellite (Sanders & Mirabel 1997), dominating the integrated light emitted by galaxies below z=0.2, the question was raised to know whether such objects, which are very bright but not numerous in the nearby universe, could be representative of a more common phase in the evolution of normal galaxies. In other words, could we expect the lack of detection of primeval galaxies (Djorgovski) to be due to dust extinction in systems emitting more than 90 % of their light in the infrared, as in local ULIRG's.

Several programs were devoted to this search using ISOCAM, one of the four instruments on board of the ISO (Infrared Space Observatory) spacecraft which ended its

Send offprint requests to: jstarck@cea.fr

life on May 1998. Operating in the range 2.5-18 μm, with a sensitivity four orders of magnitude better than IRAS and a sixty times better spatial resolution, this camera was perfectly suited for the search of dust emission in the PAH (Polycyclic Aromatic Hydrocarbon, from 6.2 to 12.7 μm) and VSG (Very Small Grains, above typically 10 μm) part of the spectrum of galaxies of redshifts typically below 1 to 1.5.

However, because the 32×32 pixels of the camera had to be both thick and cold, it had the respective consequences that they were both very sensitive to the presence of cosmic rays and slow to react to changes in fluxes. This was the main problem of faint source detection with ISOCAM which implied to discriminate non-Gaussian fluctuations of the signal from Gaussian ones, and then separate cosmic rays, i.e. glitches, from real sources. The general idea that we used for this purpose rely on the fact that all these signal components measured by a given pixel show different signatures in its temporal evolution, and can be identified using a wavelet transform, i.e. by separating several frequencies in the signal. Once the "bad" components (i.e. glitches) are identified, they can be extracted from the temporal signal. The glitch-free signal can then used to build the final image. The detection of faint sources is then performed on this final image using again a wavelet transform of the signal but this time spatially instead of temporally. We call this tool PRETI, for Pattern REcognition Technique for Isocam data, first because we use a temporal signature to recognize each signal component, which appear as a pattern in the wavelet space, but also because we were happy to finally see pretty nice images of what were previously empty fields.

In a first part, we will describe the Pattern REcognition Technique for Isocam data. Then, we will focus on the the validation of this technique using Monte-Carlo simulations. These simulations were performed on a dataset empty of real sources in which we introduced fake sources with all fluxes and positions, in order to estimate the following characteristics of an observation:

1. the sensitivity limit: the flux of the faintest detected source.
2. the photometric accuracy.
3. the completeness limit: the faintest flux for which all sources are detected or at least a well-known fraction of the total number of sources.
4. the rate of false detections: the number of fake sources due to glitches wrongly interpreted as sources.

A first set of simulations was already used in Aussel *et al.* (1999), based on the same technique, but the dataset was not empty of real sources so that the third point above could not be addressed.

2. A brief discussion of the problem

A standard way for data analysis would consist in:

1. calibrating the data:
   (a) extraction of the cosmic rays (glitches) by comparing successive readouts
   (b) subtraction of the signal due to dark currents
   (c) flat-fielding by dividing the data with a library flat-field
   (d) normalizing the camera units into real Jansky fluxes
2. using a standard source detection algorithm that would consist in estimating the background and the noise level, and fitting the Point Spread Function (PSF) in pixels showing a flux level higher than n times the noise standard deviation (rms).

This method is successful when applied to bright objects (down to a few percent of the background level) but is inefficient when applied to faint source detection (below 1 %).

At a first order, this can be improved by modeling the flat-field, instead of using the library flat-field. Indeed, the position of the lens of ISOCAM is not exactly reproducible and the optical flat-field varies as a function of the lens position of 2 to 20 % from the center to the border of the array. In the case of empty fields (and more generally when most of the map covers an empty field), a simple median of the cube of data gives a very good flat-field, which allows to reach a detection level of a few ten percent of the background level (Starck *et al.* 1998).

However, at a second order, one encounters the main difficulty in dealing with ISOCAM faint source detection: the combination of the cosmic ray impacts (glitches) and the transient behavior of the detectors. Indeed, for glitches producing single fast increase and decrease of the signal (about 20 % of the total number of readouts of an observation is thrown away because of glitches lasting only one readout), a simple median filtering allows a fairly good deglitching, while for the remaining glitches (affecting from 5 to 20 % of the total number of readouts as a function of the strength of the selection criterion), memory effects can produce false detections. Consequently, the major source of error here is not the detection limit of the instrument, which is quite low, but the large number of false detections, which increases with the sensitivity.

Three types of glitches can be isolated as they create:

1. a positive strong and short feature (lasting one readout only).
2. a positive tail (*fader*, lasting a few readouts).
3. a negative tail (*deeper*, lasting a several tens of readouts).

In the following, we will call the second type of glitches *faders*, and the third type *deepers*. Figure 1 is a plot of the camera units (ADU, for Analog to Digital Units) measured by a single pixel as a function of the number of readouts, i.e. time, which shows these three types of glitches. On top (a), three sharp type "1" glitches are clearly visible. On the middle plot (b), another pixel history shows a "fader" (at about 80 readouts and lasting about 20 readouts). On the bottom plot (c), a "deeper" is present at the readout 230, which lasts about 150 readouts.

Finally, the signal measured by a single pixel as a function of time is the combination of memory effects, cosmic ray impacts and real sources: memory effects begin with the first readouts, since the detector faces a flux variation from an offset position to the target position (stabilization), then appear with long-lasting glitches and following real sources. One needs to clearly separate all these constituents of the signal in each pixel before building a final raster map and to keep the information of the associated noise before applying a source detection algorithm. Indeed, since the glitches do not follow a Gaussian statistics, it is clear that an analysis of the final raster map, without its associated noise map, would lead to poor results, for the standard detection criterion (detection above N times the standard deviation of the noise) would no more be valid.

In a first section, we will show that a concept of pattern recognition using a multi-resolution algorithm leads to an efficient calibration procedure, free of the major problems described above. Simulations and real data analysis will be presented in a second section.

3. "Pattern recognition": a multi-scale approach

3.1. The "temporal detection technique" and its limitations

Looking at the figure 1, one can see a faint source on the bottom plot (c) at a position of about 120 readouts and lasting about 30 readouts. The duration of this bump corresponds to the time spent by the satellite when pointing on the same sky position where a source is visible. One can use this information in order to seek for real sources, since false detections induced by glitches will rarely happen at the precise moment when the satellite points toward a given direction and last exactly the number of readouts spent on this position. Moreover, by pointing twice at the same position, for example by moving of half an array per mosaic step, the probability that this happens twice should be even lower, and again lower when pointing N times at the same sky position. Figure 7 shows the case where the same source is seen by four different pixels during an observation. The dotted line separates the different mosaic positions, i.e. between two dotted lines, the same sky

position is observed. In the second and third plots, the source can easily be detected by the eye while in the two others, the signal is too noisy.

We tested an automatic "temporal detection technique" as described above and found nice results but with the following limitations:

1. *low signal to noise ratio (S/N):* in a mosaic, several pixels will point toward the same given sky position which should increase the S/N if they were co-added, which is not possible in this technique.
2. *poor photometry:* because of the previous point and also due to the difficulty to estimate the background level.
3. *sources are splitted:* the signal of weak sources extended over several pixels (either because they are intrinsically extended or because of the Point Spread Function, PSF) is splitted, resulting again in a decrease of the S/N of the source.
4. *false detections:* one still get false detections even after a redundancy of 10 or more, when searching after extremely faint objects, due to the large number of cosmic ray impacts.

In order to solve these difficulties, one needs to find the glitches with memory effects (faders and deepers) and extract them from the data, if possible without loosing the associated information. Then co-addition will become possible and standard spatial source detection algorithm with the difference that noise is not homogeneously distributed on the map. This is exactly what PRETI allows to do. In terms of noise, in the temporal technique the noise standard deviation is divided by $\sqrt{N_r}$ (where N_r is the number of readouts per raster position), while it is divided by $\sqrt{N_r} * \sqrt{N_d}$ (where N_d is the number of redundancies inside the raster, i.e. the number of pixels which see the same sky position) for co-added data.

The calibration of ISOCAM survey data can be considered under a new angle. New methods based on wavelet transforms have recently been developed for source extraction in an image (Bijaoui & Rué, 1995), and successfully adapted for spectral analysis (Starck, Siebenmorgen & Gredel, 1997). Using such an approach, a temporal signal can be decomposed in its different components, selected from their frequency. From this decomposition, a new calibration method can be derived, resolving main problems.

3.2. The Multi-Scale Vision Model

In the Multi-Scale Vision Model (Bijaoui & Rué, 1995), an object in a signal is defined as a set of structures detected in the wavelet space. The wavelet transform algorithm used for such a decomposition is the so-called "à trous" algorithm, which allows to represent a signal $D(t)$ by a simple sum of its wavelet coefficients w_j and a smoothed version of

the signal c_p

$$D(t) = c_p(t) + \sum_{j=1}^{p} w_j(t) \tag{1}$$

In the case of an image of the sky, the algorithm would produce N images of the same size, each one containing only information at a given frequency band. In such images, we define a "structure" as a group of connected significant (above a given threshold) wavelet coefficients. A complete description of how to estimate if a wavelet coefficient is significant, depending on the nature of the noise, can be found in Starck, Murtagh & Bijaoui (1995) and Starck, Murtagh & Bijaoui (1998). An object is described as a hierarchical set of structures. The law will allows us to connect two structures into a single object is called "interscale-relation". Figure 3 shows how several structures in different scales are linked together, and form objects. We have now to define the interscale-relation: let us consider two structures at two successive scales, S_j^1 and S_{j+1}^2. Each structure is located on one of the individual images of the decomposition and corresponds to a region in this image where the signal is significant. Noting p_m the pixel position of the maximum wavelet coefficient value of S_j^1, S_j^1 is said to be connected to S_{j+1}^2 if S_{j+1}^2 contains the pixel position p_m (i.e. the maximum position of the structure S_j^1 must also be contained in the structure S_{j+1}^2). Several structures appearing on successive wavelet coefficient images can be connected in such a way, which we call an object in the interscale connectivity graph.

Once an object is detected in the wavelet space, it can be isolated by searching for the simplest function which presents the same signal in the wavelet space.. The problem of reconstruction (Bijaoui and Rué, 1995) consists then in searching a signal V such that its wavelet coefficients are the same than those of the detected structure. By noting $\mathcal{T}$ the wavelet transform operator, and P_b the projection operator in the subspace of the detected coefficients (i.e. set to zero all coefficients at scales and positions where nothing was detected), the solution can be found by minimizing the following expression:

$$J(V) = \| W - (P_b \circ \mathcal{T})V \| \tag{2}$$

where W represents the detected wavelet coefficients of the signal. A complete description of algorithms for minimization of such a functional can be found in Bijaoui & Rué (1995).

In ISOCAM images, cosmic rays with memory effects are the typical objects as previously described, but instead of working on the spatial signal of an image, one needs to work on the time sequence of the signal to find them. Indeed, the signal associated to a fader or a deeper is significant at several frequencies: a strong and rapid peak make them significant in the highest frequency wavelet coefficients decomposition of the initial signal while the memory effect make them significant in the lower frequency wavelet coefficients. Hence, the multi-scale approach is an ideal tool to discriminate glitches from real

signal and we will call pattern recognition, the action of searching for objects showing properties typical of those expected for faders and deepers.

3.3. Pattern REcognition Technique for Isocam

The idea developed here is to use the multi-scale vision modeling for a decomposition of a signal into its principal components. In practice, a simple object reconstruction from the detected structured in the wavelet space, as proposed in Bijaoui & Rué (1995), would produce poor results because of the strong confusion between the numerous objects that can be found in the data. Moreover, wavelet transforms present a drawback: the wings of the wavelet function are negative (so that integral of the function is zero) which implies that when a positive signal falls onto one wing of the wavelet function it produces a negative signal in the wavelet transform. The quality of the object reconstruction is good only when additional constraints are introduced (positivity constraint for positive objects, and negativity constraint for negative objects). An object is defined as positive (respectively negative) when the wavelet coefficient of the object which has the maximum absolute value is positive (respectively negative).

The problem of confusion between numerous objects can be solved when including a selection criterion in the detection of these objects. Using the knowledge we have about the objects, here glitches, the problem of unknown objects reconstruction is reduced to a pattern recognition problem, where the pattern is the glitch itself. We only search for objects which satisfy a given set of conditions in the Multi-Scale Vision Model (MVM). For example, finding glitches of the first type is equivalent to find objects which are positive, strong, and with a duration lower than those of the sources. The method that we use for the decomposition of the signal of a given ISOCAM pixel, $D(t_0..t_n)$, is summarized below:

1. detection of the glitches of the first type in the wavelet space: the corresponding signal, $C_1(t_0..t_n)$, is then subtracted to the initial data, D: $D_1 = D - C_1$. This is the first step of deglitching.
2. detection of the negative components due to deepers: the multi-scale vision model is applied to D_1, hence negative objects are detected and the reconstructed signal, $C_2(t_0..t_n)$, is then subtracted to the output of the previous step: $D_2 = D_1 - C_2$. This is the second step of deglitching where troughs following glitches are corrected.
3. detection of the positive components due to faders and deepers: this step must be done carefully, since sources also produce positive components in the signal, but only positive object lasting much more or much less than the time spent on a given position of the mosaic on the sky, i.e. the duration of a real source, are automatically considered

as glitches. The output signal, $C_3(t_0..t_n)$, is then subtracted again to the previous signal: $D_3 = D_2 - C_3$.

4. detection of very strong positive signal at scales where sources are expected. This step is done in preparation of the baseline subtraction (the final source detection is not done at this stage). The multiscale vision model is applied to D_3 and strong positive objects with a correct temporal size are reconstructed: we get $C_4(t_0..t_n)$, and we calculate $D_4 = D_3 - C_4$.
5. subtraction of the baseline: the signal D_4 contains only noise and temporally undetectable faint sources. The baseline is easily obtained by convolving D_4 by a low frequency pass band filter. We get $C_5(t_0..t_n)$.
6. The residual noise is obtained by $C_6 = D_4 - C_5$, its mean value is zero.

Finally, the set $(C_1, C_2, C_3, C_4, C_5, C_6)$, represents the decomposition of the signal into its principal components. Note also that the input signal D is equal to the sum of all components:

$$D = \sum_{i=1}^{6} C_i \tag{3}$$

A complete deglitching (all types of glitches) is obtained by:

$$D_g = D - C_1 - C_2 - C_3 \tag{4}$$

For the faint source detection, we use the signal $D_b = C_4 + C_6$, which is background, dark, and glitch free. The background has been subtracted, and glitches with their long duration effects have been suppressed. Applying the pattern recognition method to all detector pixels, we obtain a cube $D_b(x, y, t)$. All other component are kept in the cubes C_i. The baseline suppression presents several advantages: firstly, the final raster map will be dark-corrected without the need of a library dark, since we end up with a mean zero level for each pixel. This is particularly important when the library dark is not good enough, and visual artifacts often remain (see Siebenmorgen *et al.* 1996). Secondly, the calibration is less affected by the flat-field accuracy, which only affects the photometry of the sources but not the background level, which is extracted in the baseline.

3.4. Example

Figure 4 (bottom) presents the result after applying such a treatment. The decomposition of the original signal (figure 4 top) into its principal components is shown on Figure 5: (a), (b), and (d) are features subtracted from the original signal (a: short glitches, b: trough of a deeper, d: baseline), which present no direct interest for faint source detection, and only (c) and (e) (c: bright sources and e: noise plus faint sources) are kept for building the final image. The noise must also be kept because faint sources could be undetectable in a

single temporal signal, but detectable after co-addition of the data. The simple sum of the fives components is exactly equal to the original data (see figure 4 top). The calibrated background free data (see figure 4 bottom) are then obtained by addition of (c) and (e).

3.5. Downward transient correction

Three kinds of transients must be distinguished:

1. a long term transient at the beginning of the observation. It can be either a downward or an upward transient due to the fact that the detector was illuminated by another flux before the observation began, which can be lower or higher than the present flux. If the difference between the present background level (which dominates the signal in observations looking after faint sources) and the previous background level is high, then the transient effect can affect several hundred of frames. Long term transients have no effect for source detection when using the multi-resolution approach, because they are eliminated with the baseline.
2. an upward transient each time a pixel points in the direction of a sources. There is presently no physical model which describes the ISOCAM upward transient. This kind of transient affects mainly the photometry. Objects with a flux at the theoretical detection limit will not be detected because the signal measured is only a fraction (typically 60 %) of the signal after stabilization (too long to be waited for).
3. a downward transient after each source, which can produce ghosts when following bright sources, since the downward transient may remain above the noise even after the change of position in the mosaic.

For an automatic source detection, the last kind of transient must be corrected for. Physical models do exist for downward transients and several methods may be used (see Siebenmorgen *et al.* 1996, Abergel *et al.* 1996 for a description of these methods). In our case, a very trivial approach can also be used, which consists in treating the reconstructed temporal objects. Indeed, we can assume that the part of the object which appears after the displacement in the mosaic is the transient, and it can be eliminated by a simple thresholding.

Figure 6 shows the result after such a treatment: (top) a signal containing a source. The downward transient is relatively strong in this case, and three successive positions on the mosaic are affected by the transient, inducing ghosts in the final image if they are not removed. The signal after deglitching and baseline subtraction is plotted in figure 6 (middle), and the result after the downward transient correction is shown in figure 6 (bottom). The shape of the source is due to the upward transient correction which will correct using the technique developed by Abergel *et al.* (1996).

3.6. Conclusion

This solution produces good results but requires a long computation time. A similar but faster method, producing as good results too and avoiding the delicate problem of the negative wings of wavelet functions, is to use the Multi-Resolution Median Transform (MMT) (see Starck *et al.* 1996, for a description of the algorithm) instead of the wavelet transform. No confusion between positive and negative objects is possible because this multi-resolution transform does not present the ringing drawback. Furthermore, the object reconstruction is straightforward, because no iteration is needed to get a good quality reconstruction. Once the calibration is done, the raster map can be normally created, with flat field correction, and all data co-added. The associated rms map can now be used for the detection, which was impossible before due to the strong effect of residual glitches. Since the background was removed, a simple source detection can be done just by comparing the flux in the raster map to the rms map.

4. Object Detection

Once all data have been calibrated, the final raster map $R(x, y)$ and its associated rms map $R_\sigma(x, y)$ can be created. If several rasters of the same field are available, they can be co-added in order to improve the signal to noise ratio. The noise in $R(x, y)$ (i.e. $R_\sigma(x, y)$) is non homogeneously distributed over the map, firstly because some pixels have been masked (short glitches) and secondly because some areas of the field (particularly the border of the mosaic) present less redundancy (less readouts per sky position). Assuming the simple hypothesis of a Gaussian and uniform noise would lead to a large amount of false detections on the border. The only solution is to use the $R_\sigma(x, y)$ map. In order to detect faint sources on the final image, the multi-scale vision model (Bijaoui & Rué 1995) described in section 3.2 can again be used (but spatially this time), but the correct noise model must be considered. For each wavelet coefficient $w_j(x, y)$ of R, the exact standard deviation $\sigma_j(x, y)$ have to be calculated from the root mean square map $R_\sigma(x, y)$.

A wavelet coefficient $w_j(x, y)$ is obtained by the correlation product between the image R and a function g_j:

$$w_j(x, y) = \sum_k \sum_l R(x, y) g_j(x + k, y + l) \tag{5}$$

then we have:

$$\sigma_j^2(x, y) = \sum_k \sum_l R_\sigma^2(x, y) g_j^2(x + k, y + l) \tag{6}$$

In the case of the à trous algorithm, the coefficients $g_j(x, y)$ are not known exactly, but they can easily be computed by taking the wavelet transform of a Dirac w^δ. The map σ_j^2 is calculated by correlating the square of the wavelet scale j of w^δ by $R_\sigma^2(x, y)$.

A wavelet coefficient is significant if:

$$| w_j(x,y) | > N_\sigma \sigma_j(x,y) \tag{7}$$

N_σ is a parameter fixing the level of confidence (generally taken equal to 3). Once this step is performed, the objects selection and their reconstructions can be done as described in Bijaoui & Rué (1995). One can therefore produce a map containing only the reconstructed objects, i.e. the sources (galaxies, stars) that we were looking for. This fits image can be used for comparison to other wavelengths.

Finally, the outputs of PRETI are numerous and contain all information at all scales divided into several cubes of data and fits images, but the most commonly used outputs are the following:

1. the final fits image and its rms image associated.
2. the fits image of the reconstructed objects
3. the list of objects with their position, flux and flux error (assuming no transient error), the sigma level of the detection and the scale at which the object was detected (size of the object).

The confidence level associated to the faint sources detected with PRETI cannot be directly understood as an usual signal-to-noise ratio typical of a Gaussian noise. Indeed, due to the presence of remnant glitches, the detection level is not fixed by the overall rms but by the level at which false detections begin to appear. One way to check the robustness of the source detection consists in keeping only sources much above the detection limit, in order to avoid introducing false detections and when overlaid on optical images one can clearly check that the list of sources that he selected corresponds to real objects on the sky. However, if one wants to get the faintest objects possible and still be sure to avoid introducing false detections, the only solution is to introduce fake sources in real ISOCAM data and analyses a set of simulated data for different flux levels and sources densities. Such simulations were performed to allow the determination of number counts plots. They are described hereafter.

5. Simulations

The behavior of the noise in ISOCAM data is not Gaussian because of the presence of glitches which modify the response of the detectors over several tens of readouts and adds to the standard Gaussian noise produced by the readout noise and the photon noise. In order to check the robustness of the source detection, we preferred to use real ISOCAM data for the simulation of a mosaic with given fake sources instead of trying to build a set of simulated data from scratch with the uncertainty linked to the lack of understanding

of the effect of glitches on the detectors. The main objectives of these simulations are summarized below:

1. *the sensitivity limit:* the flux of the faintest detected source. Sources detected down to this flux level cannot be used for number counts, since only a fraction of these sources will be detected.
2. *the photometric accuracy:* detectors generally do not stabilize when pointing towards faint sources because it would be too much time consuming. Hence the uncertainty on the photometry depends on the quality of the algorithm for transient correction (Abergel *et el.* 1996, a new version of this code is being tested at the present time, which appear to give impressive results and may reduce the photometric uncertainty down to a few percent even for faint sources). This uncertainty can be quantified using simulations including sources with a well-known flux and a simulated transient behavior.
3. *the completeness limit:* the faintest flux for which all sources are detected. Monte-Carlo simulations will be useful to give constraints on the number counts at a given flux level below the completeness limit by quantifying the fraction of galaxies that may have been missed down to this flux.
4. *the rate of false detections:* the number of false detections due to glitches wrongly interpreted as sources.

5.1. Simulation of fake sources

An ideal source is a step function, i.e. the signal of a pixel increases when observing the source and after decreases down to the background level. The presence of transients modifies this behavior. We used the Abergel *et al.* (1996) transient model to simulate the sources as seen by ISOCAM. To take into account the PSF effect, i.e. the distribution of the flux of a point source among the nearby pixels, we adopted the Okumura (1997) model. In this way we are able to simulate a source once its position on the detector is known. An observation is therefore composed by a set of sources which positions follow a uniform probability density function.

To study the completeness limit and the photometric accuracy, one can generate a list of sources all of which have the same flux. Several lists have to be generated in order to avoid that peculiar source positions (e.g. a pixel affected by a lot of glitches) could affect the result. Fake observation data are then created for several flux levels. This method was applied in the study of the ISOCAM image of the Hubble Deep Field (Aussel *et al.*. 1998) but no direct check of the rate of false detections was possible at that time (we used the real dataset with real sources in it), while we will present below as an example a study on a dataset empty of real sources: a staring observation was performed over

a long time and then analyzed as if it was a mosaic, hence real sources could easily be extracted when subtracting the baseline of the signal in each pixel, since a real source would last all along the staring observation.

To test if from an observation we can recover the number counts ($\log N - \log S$ or dN/dS) expected for the population observed in the field, we can analyze simulated observations which contain random lists of fake sources whose fluxes follow the theoretical $\log N - \log S$. We will apply this method to the case of the Hubble Deep Field (see below).

5.2. Noise and cosmic rays simulation

Instrumental noise and cosmic ray effects have to be added to each pixel signal. Due to our ignorance about the effects on the detector of cosmic rays, we are compelled to use real ISOCAM data. A first possibility is to add fake sources to the real observation: this allows to test and calibrate the photometry and verify the completeness at a given flux by comparing the number of new detections with the number of fake sources introduced. However, this technique does not allow to measure the false detection rate and to test the possibility to recover a $\log N - \log S$ if this relation is sensitive to the confusion. This is possible only if we use an observation without sources in it, where the only sources are the fake sources intentionally added to the dataset. An observation of this kind is obtained by using the data of a unique very long pointed observation ("staring" observation) and cutting it to create a fake "raster" observation (i.e. a mosaic observation). In this way, if a pixel sees a source, its flux will be a bit higher than the background along all the observation, which has no effect on the source detection algorithm since the low frequency signal is subtracted.

The "staring" observation has to be at least as long as the mosaic to simulate. Moreover, the rate of cosmic rays has to be compatible with that of the observation and the integration time has to be the same, since the behavior of the detectors depends on this time. Finally, the high frequency photon noise of the two observations has to be compatible. Such long staring observations have been performed just before the end of the mission using the calibration time, in the two main ISOCAM filters (LW2 and LW3) which we used as base of simulation.

5.3. Specificity of a simulation

Ideally, if one wants to reach the very limit of the instrument, a new set of simulations should be produced and analyzed per observation, since the results depend on the parameters of the observations as well as on the background level and glitch rate. However, typical cases can be analyzed and used as templates for other observations. We have performed detailed simulations (one hundred simulations per observation) for two tem-

Table 1. Comparison of the noise level and rate of cosmic rays between the ISO-HDF observation and a staring observation used for building a simulation of the same ISO-HDF mosaic in the LW3 band (12-18 μm).

Observation	ISO-HDF	Simulation
Noise level (ADU/G/s)	0.229	0.232
Masked pixels	19.4 %	19.1 %
Corrected pixels:	19.3 %	18.9 %
Faders	5.2 %	5.5 %
Dippers	14.1 %	13.4 %

plate cases: the "ISO-HDF", on one hand (see below), which corresponds to what we call ultra-deep observations with a very large redundancy, and the "Deep Survey", on the other hand (in a forthcoming paper, see also Elbaz *et al.* 1998), for shallower observation with less redundancy and spatial resolution.

6. The case of the Hubble Deep Field

This work completes a previous paper on the ISO-HDF (Aussel *et al.* 1998) by new simulations on an ideal dataset at 15 μm (filter LW3, 12-18 μm, see Figures 7,8,9). In order to check if the conditions were similar for both observations (the staring observation and the real mosaic on the HDF field), we performed a first analysis of the staring observation in order to get the percentage of readouts lost because of glitches of type 1 (short glitches inducing a one readout peak that will be masked out), and types 2 and 3 (faders and deepers). In the case of the ISO-HDF (see Table 1), the percentage of data corrected because of faders and deepers makes a total of about 20 %, close to the fraction of pixels masked because of glitches of type 1. In the case of Deep Survey-like observations, for comparison, the redundancy per sky position being much lower (about 3-6, instead of 64), one cannot set such strong criteria for the correction of glitches with memory effects and the typical fraction of corrected pixels is of the order of 5 % (the fraction of masked pixels, however remains identical). Finally, we also checked that the mean Gaussian plus readout noise, making the Gaussian part of the noise is comparable in both observations, which is indeed the case when considering the same integration time as shown in Table 1.

In order to quantify the effect of incompleteness plus photometric uncertainty on the number counts, we built several ISO-HDF simulated images including fake sources which flux distribution followed the one described in Franceschini *et al.* (1997). We would like to stress here that this does not influence the output number counts as if we had put in

entrance what we were looking for in output, but on the contrary it allowed us to check if after applying PRETI the slope of the number counts was close to the one we had used. The main uncertainty here comes from the accuracy reached in the photometry of the sources, which will redistribute the sources in each flux bin.

We used a lower limit of $S_l = 0.1\mu Jy$, which is much lower than the sensitivity of our observations, and an upper limit $S_u = 1mJy$, for the fluxes of the fake sources. We then simulated several fake mosaics with a distribution of fluxes following the distribution described above. Fluxes in Jy were converted into ISOCAM units (ADU/gain/second) following the standard conversion table from the ISO cookbook (ISO Team, 1994: 1 ADU/g/s = 1.96 mJy with LW3).

We projected each source on the detector for each pointing of the camera by taking into account the field distortion and the point spread function (using the model of Okumura 1997). This allowed us to build a cube of images, i.e. an image of 32x32 pixels for each pointing of the satellite, that we multiplied by the flat-field computed from the original data without fake sources. Finally, we added to this cube the mean background level of the staring in order to model the transient behavior of the sources, which depends on the total flux level of each detector, using the model of Abergel *et al.* (1996). Finally, we subtracted again the mean background level to this cube of fake sources in order to add it to the real dataset of the staring observation, which contains the real background with noise and cosmic rays.

Figure 7 shows the fraction of false detections as a function of the flux limit using a detection threshold of $7\tau_w$ and $5\tau_w$, where τ_w is the noise level in the wavelet space (we preferred to use this term instead of Nσ in order to avoid confusion due to the complexity of the noise). For each simulation, we have built a main and a supplementary list of sources as mentioned in the paper and found that in both cases the rate of false detection down to the completeness limit is only 2 %.

Hence in the main list of sources extracted from the ISO-HDF (21 sources), which was built using the $7\tau_w$ threshold, the completeness limit is 200 μJy while the sensitivity limit is 50 μJy with a rate of false detection close to 2%. But in the supplementary list (a total of 46 sources including the previous list), which goes down to $5\tau_w$, the completeness limit is 100 μJy with about the same rate of false detection of 2 %, which we could not measure previously. Hence, we can now merge these two source lists into one single list of 46 sources which completeness limit is 100 μJy instead of twice more, which contains statistically one single false source (2% of 46 sources) with a confidence level of 95%. At fainter fluxes, the number of false detections increases very rapidly in the supplementary list. For a limit of 20 μJy it varies between 5 and 30% according to the simulations. On a list of one hundred sources this means 10 false detections between 20 and 80 μJy.

7. Conclusion

We have developed a tool for faint sources detection in ISOCAM data, which proved to be particularly well adapted for the detection of sources at the few tens μJy level in the presence of glitches with memory effects. We created simulated datasets in order to test the robustness of the technique and found a quantitative way to estimate the quality of source lists extracted from deep surveys, while the signal-to-noise ratio alone would be misleading. We applied this technique to a simulation of the ISO-HDF and found that the completeness limit at 15 μm is 100 μJy with 2 % of false detections due to remnant glitches. New results already obtained with PRETI will follow this paper in the near future.

References

Abergel, A., Bernard, J.-P., Boulanger, F., *et al.*, 1996, A&A, 315, L329

Aussel, H., Cesarsky, C. J., Elbaz, D. & Starck J. L., 1998, A&A , in press

Aussel H., 1998, Thesis, Université d'Orsay, France.

Bijaoui, A., Rué, F., 1995, Signal Processing, 46, pp 345–362.

Désert, F.X., Puget, J.-L., 1996, ISOCAM: Reduction technique for deeps survey, IAS Orsay technical report.

Désert, F. X., Puget, J.-L., Clements, D., 1998, A&A, in press.

Elbaz, D., *et al.*, 1998, invited contribution to Proc. of 34th Liege International Astrophysics Colloquium on the "Next Generation Space Telescope", ESA Publication, astro-ph/9807209

ISO Team, 1994, 'ISOCAM Observer Manual', http://isowww.estec.esa.nl/manuals/iso_cam/cam_om_1.html.

Okumura, K., 1997,ISOCAM PSF Report, ESA/CAM IDT, http://isowww.estec.esa.nl:80/instr/CAL/cal_wksp.

Siebenmorgen, R., Starck, J.L., Cesarsky, D.A., Guest, S., Sauvage, M., "ISOCAM Data Users Manual Version 2.1", ESA Document, Reference: SAI/95-222/Dc.

Starck J.L., Murtagh F. , and Bijaoui A., 1998 "Image Processing and Data Analysis in the Physical Sciences: The Multi-Scale Approach", Cambridge University Press, Cambridge (GB).

Starck J.L., Siebenmorgen R., and Gredel R., 1997, Astrophysical Journal, Vol. 482, pp 1011–1020.

Starck, J.L., Murtagh, F., Pirenne, B., and Albrecht, M., 1996, PASP, 108, pp 446–455.

Starck J.L., et al, A&A, 133, 1998.

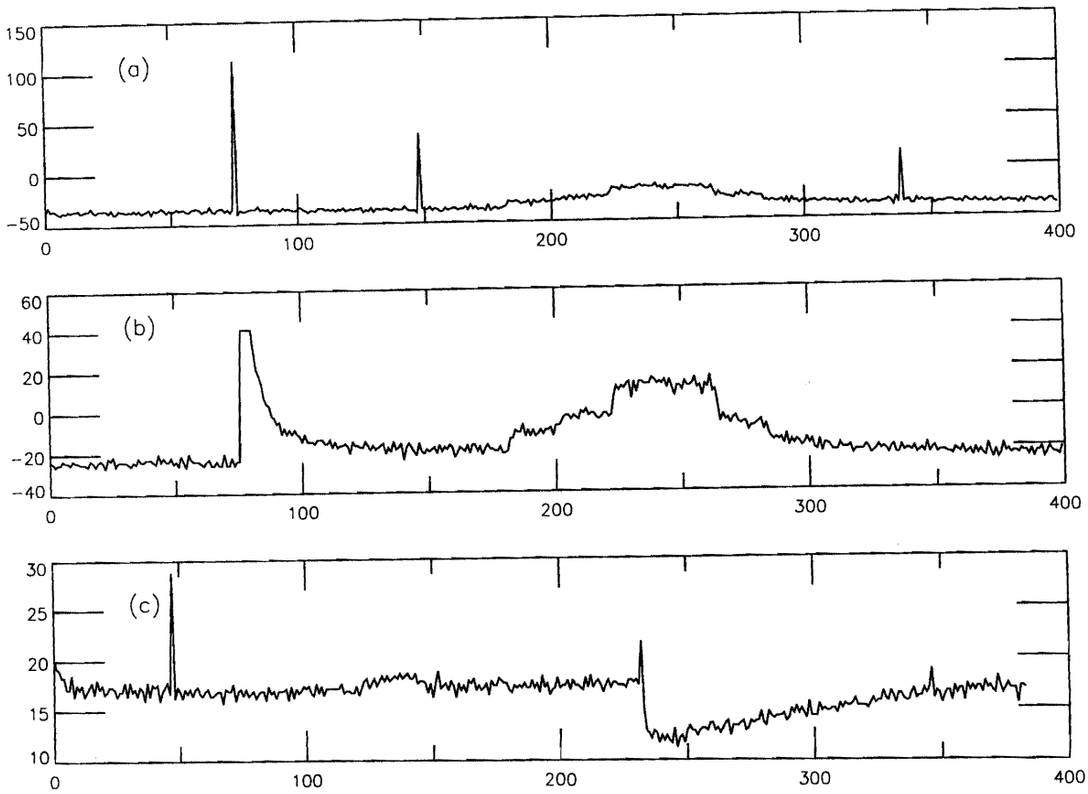

Fig. 1. Those three plots show the detector response in Analog to Digital Units (ADU) as a function of time, expressed here in number of readouts. Three types of cosmic rays (or glitches) can be found here: (a) top: the most common glitches, lasting only one readout. (b) middle: a "fader", around readout 80. This glitch presents a slowly decreasing tail. It has been truncated above 40 ADUs, but its original intensity is 2700 ADUs. (c) bottom: a "deeper", around readout 240. This glitch is followed by a trough lasting about 100 readouts. In these observations, the camera draws a mosaic on the sky, hence as long as an object, like a star or a galaxy, is in the line of sight of a given pixel, the measured signal increases. One can clearly see a bump in the signal of the middle plot (b) around the readout 180, which results from the presence of an extended source seen on 2 adjacent positions of the mosaic (first position: from readout 180 to readout 220; second position: from readout 220 to readout 260) and then followed by a transient signal due to memory effect up to the readout 300. This bump is produced by a galaxy extended over 2 positions of the mosaic. A fainter galaxy is visible on the bottom plot (c) around readout 120, lasting only one mosaic position.

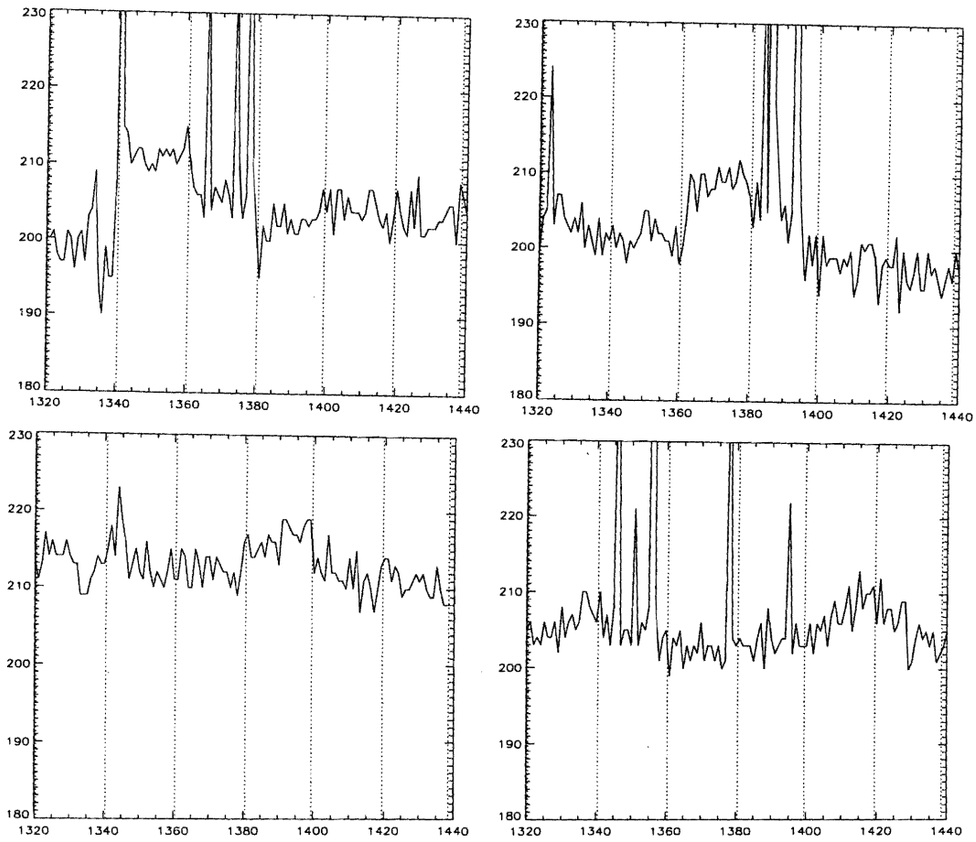

Fig. 2. Four pixel histories (top left pixel (4,12), top right pixel (12,12), bottom left pixel (20,12), and bottom right pixel (27,12)). The ADU is plotted versus the readout number. The dotted line indicate when the satellite moved (i.e. between two dotted lines, the observed flux is the same). The same source is seen by the four pixels respectively at position 2,3,4,5. It can be relatively easily detected in pixel (12,12) and (20,12), while it is more difficult to see it in pixels (4,12) and (27,12).

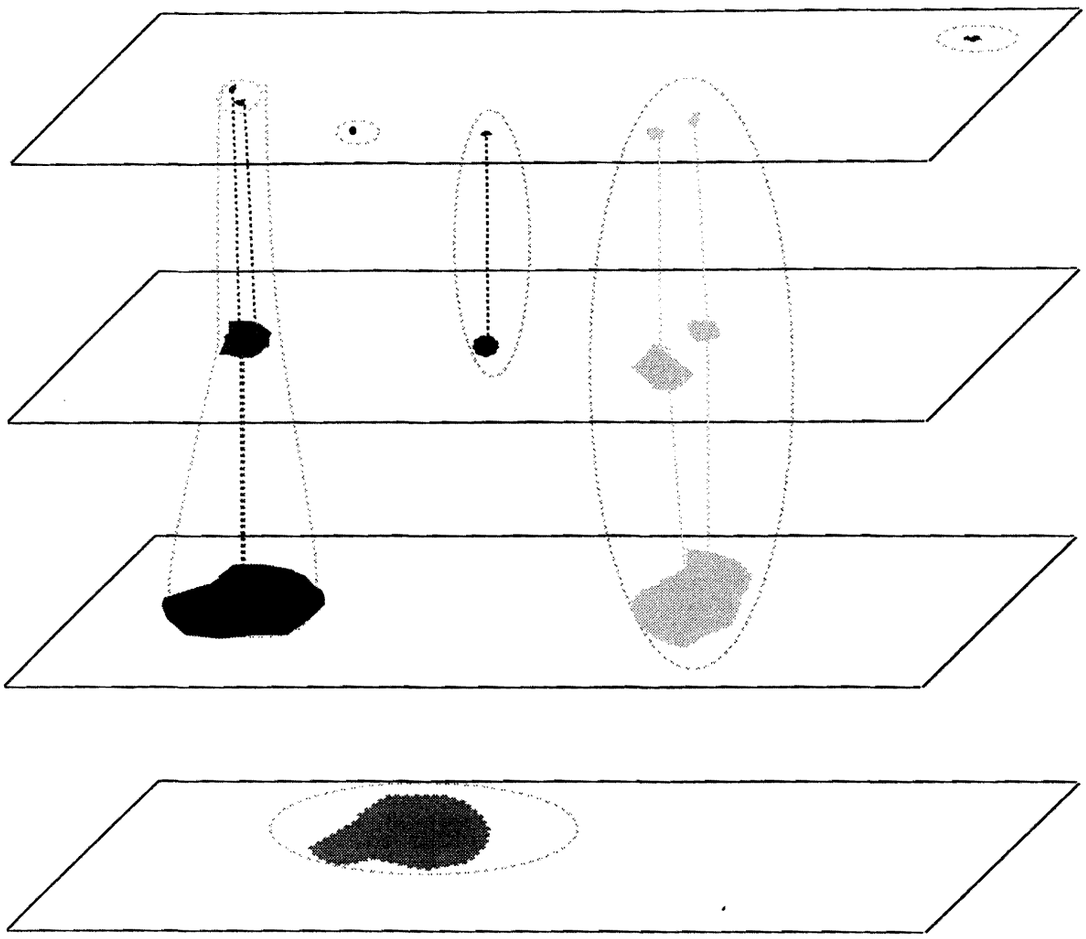

Fig. 3. The Multiscale Vision Model: contiguous significant wavelet coefficients form a structure, and following an interscale relation, a set of structures form an object. Two structures S_j, S_{j+1} at two successive scales belongs to the same object if the position pixel of the maximum wavelet coefficient value of S_j is included in S_{j+1}.

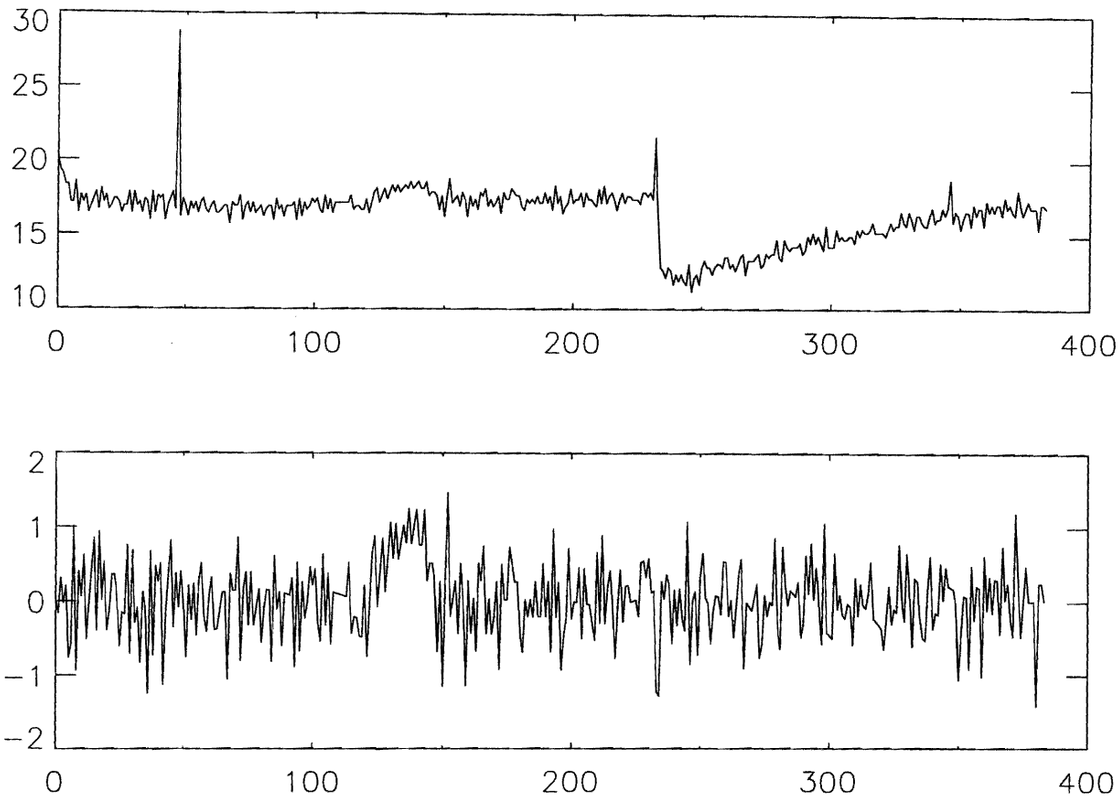

Fig. 4. These two plots show the signal of a single pixel as a function of time before calibration (top, flux in ADU) and after calibration (bottom, flux in ADU/gain/second). The trough following the second glitch (deeper) has disappeared and the remaining signal contains only Gaussian noise (photon noise + readout noise) plus sources (one relatively bright source is located at readout 120, fainter sources will only appear after co-addition of all pixels having seen the same sky position on the final map).

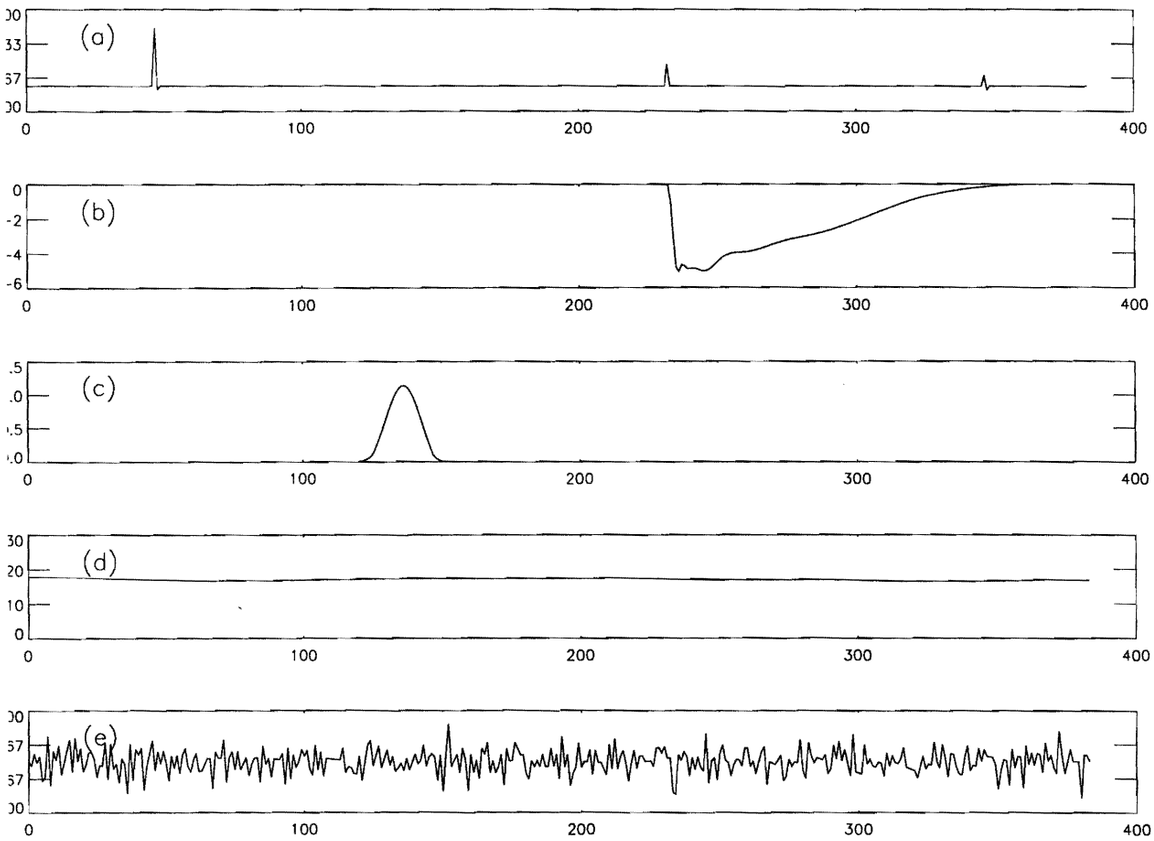

Fig. 5. Decomposition of the signal into its principal components: (a) short glitch, (b) trough of a deeper, (c) bright source, (d) baseline, (e) noise plus faint sources. The simple sum of the fives components is exactly equal to the original data (see figure 2). The calibrated background free data are obtained by addition of signals (c) and (e). Plot (c) shows the reconstruction of a source approximated as a Gaussian, but sources are kept in the signal and their shape differ from one source to the other

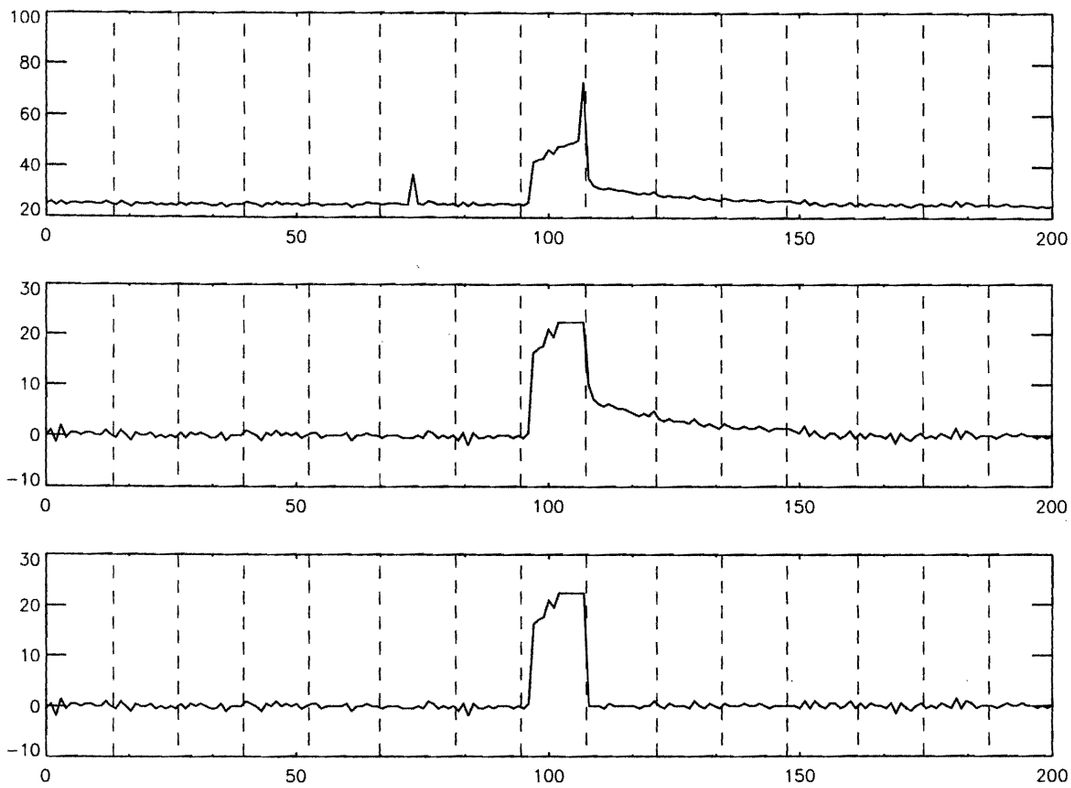

Fig. 6. Examples of transient correction. (top) signal containing a strong source. Dashed line shows the configuration limits. (middle) deglitched Signal without any baseline. (bottom) deglitched Signal without any baseline, and after transient correction.

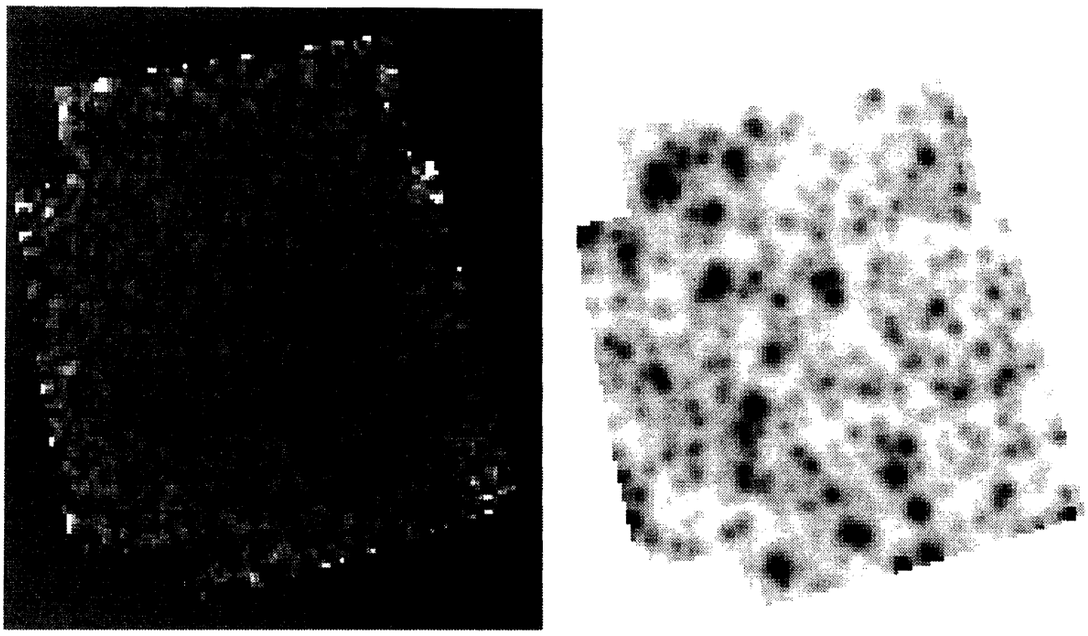

Fig. 7. simulation of the ISO-HDF mosaic (I): (left) this image contains only simulated photon noise plus readout noise, i.e. gaussian noise, (right) image of the ISO-HDF mosaic without any noise and with a distribution of sources following the no evolution model of Franceschini et al. 1997 (sources with a flux ranging from $0.1\mu Jy$ to $1mJy$).

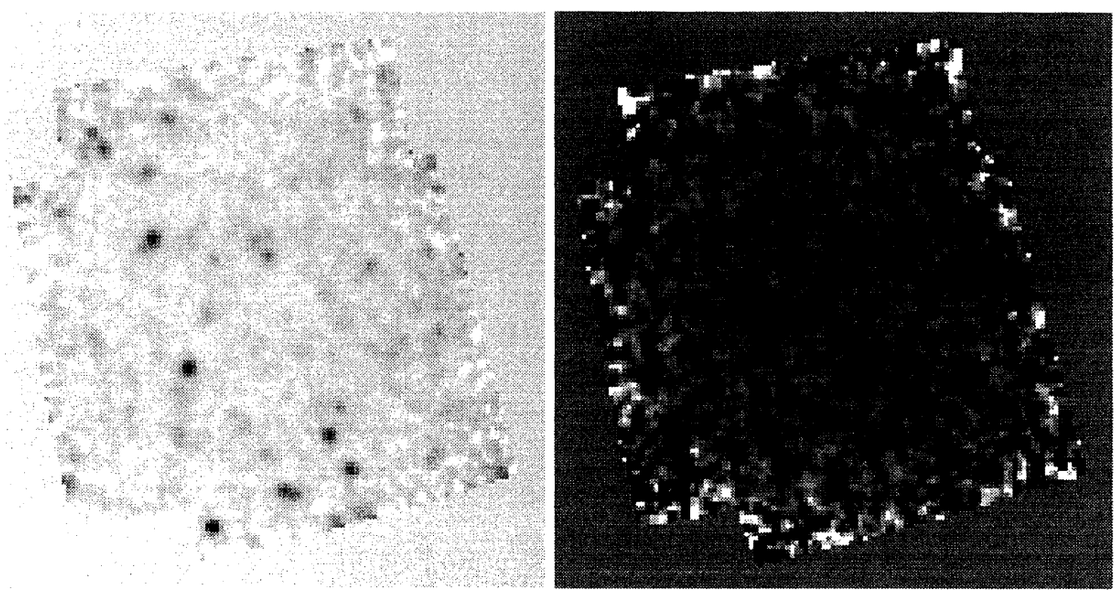

Fig. 8. simulation of the ISO-HDF mosaic (II): (left) sum of the two previous images, i.e. simulated sources plus readout and photon noise, (right) image of the ISO-HDF mosaic simulated from a staring observation, i.e. all sources of noise are present but no source at all (this image can be used to estimate the number of false detections due to glitches, since it does not contain any real source).

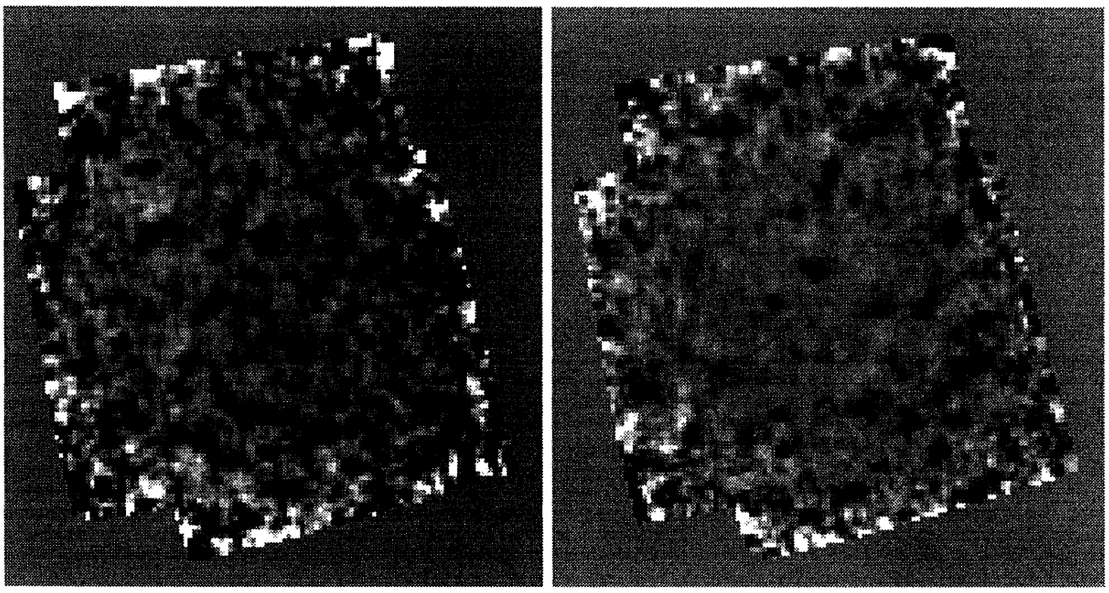

Fig. 9. ISO-HDF mosaic: (left) full simulated ISO-HDF image using the staring observation plus a distribution of fake sources following the no-evolution model of Franceschini et al. 1997, i.e. sum of fig.8(right) plus fig.7(right), (right) real image of the ISO-HDF. We find more sources in the real image than in the simulated image, indicating strong evolution.

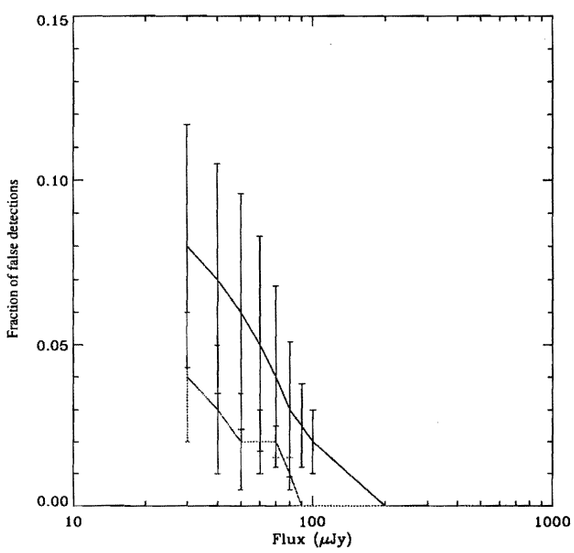

Fig. 10. Fraction of false detections as function of the limit flux of the sample, for a detection threshold of 7 τ_w (lower) and 5 τ_w (upper).